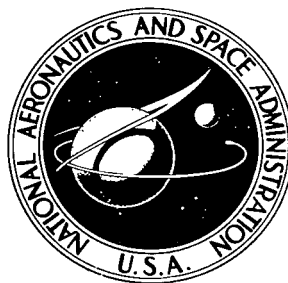


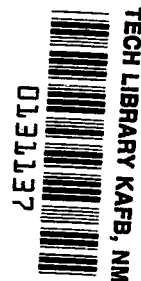
NASA TECHNICAL NOTE



NASA TN D-4530

2.1

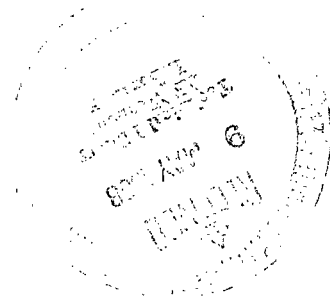
NASA TN D-4530



LOAN COPY: RETURN TO
AFWL (WLIL-2)
KIRTLAND AFB, N MEX

FLIGHT INVESTIGATION OF A CAPACITANCE-TYPE METEOROID DETECTOR USING AN INFLATABLE PARAGLIDER

by James H. Siviter, Jr.
Langley Research Center
Langley Station, Hampton, Va.





FLIGHT INVESTIGATION OF A CAPACITANCE-TYPE METEOROID DETECTOR
USING AN INFLATABLE PARAGLIDER

By James H. Siviter, Jr.

Langley Research Center
Langley Station, Hampton, Va.

NATIONAL AERONAUTICS AND SPACE ADMINISTRATION

For sale by the Clearinghouse for Federal Scientific and Technical Information
Springfield, Virginia 22151 - CFSTI price \$3.00

FLIGHT INVESTIGATION OF A CAPACITANCE-TYPE METEOROID DETECTOR USING AN INFLATABLE PARAGLIDER

By James H. Siviter, Jr.
Langley Research Center

SUMMARY

One of the meteoroid-detection systems under development at the Langley Research Center consists of thin-film multiple capacitors made of layers of aluminized poly(ethylene terephthalate) (PET). The capacitor momentarily discharges when penetrated by a hypervelocity projectile. The multilayer capacitor-type detector used in this experiment was designed to detect particle penetrations in 6.5, 20, and 45 microns of PET.

Eighteen square meters of the micrometeoroid-detector material was attached to the wing of an inflatable paraglider. The paraglider provided a convenient mounting structure for the sensors and a means of recovering the sensors after the flight test. The packaged paraglider and sensors were boosted to an altitude of 93 kilometers where the paraglider was ejected and inflated. The inflated paraglider then continued along a ballistic trajectory to a maximum altitude of 154.7 kilometers. Sensor data were recorded for approximately 169 seconds at altitudes above 121 kilometers. The excessive noise on the telemetry-data channels made exact analysis of the penetration data inconclusive.

The deployment and inflation of the paraglider were normal and it attained the proper flight attitude during reentry; however, the telemeter section failed to release, and, as a result, the reentry loads were excessive. Large sections of the wing membranes containing the micrometeoroid-detection sensors were lost during reentry; thus, extensive laboratory examination of the sensors for craters is prohibited.

INTRODUCTION

The Langley Research Center with support from the Goddard Space Flight Center flew a micrometeoroid experiment from White Sands Missile Range with the use of an Aerobee 150 sounding rocket. The primary objectives of the experiment were to obtain data on the performance during flight of a multilayer thin-film capacitor-type meteoroid penetration detector and to obtain data on the penetration rates of the very small mass micrometeoroids in near-earth space. The capacitor-type penetration detectors were

mounted on an inflatable paraglider that could be recovered; thus, additional data on the sensor performance could be obtained by postflight visual inspection. A secondary objective of the experiment was to obtain data on the reentry capability of the inflatable paraglider.

This report presents the background and a description of the meteoroid experiment; describes the capacitor-type penetration detector, the launch vehicle, and the inflatable paraglider used; and discusses the data resulting from the experiment.

BACKGROUND AND DESCRIPTION OF EXPERIMENT

The Langley Research Center has been involved since 1955 in research and development activities aimed at defining the meteoroid hazard to spacecraft. These activities have included laboratory investigations of the damage resulting from the impact of high-speed particles, and flight experiments to measure directly in space the meteoroid-penetration rates in various materials and material thicknesses. The S-55 series of micrometeoroid satellites (refs. 1 and 2) that involved the development of an earth-orbital spacecraft instrumented with pressurized-cell penetration detectors was the first Langley project involving meteoroid flight experiments. The S-55 series measured the meteoroid penetrations in metals 25 and 50 microns thick. The pressurized-cell-type penetration detectors used in the S-55 series cannot be used to measure penetrations in materials much thinner than 25 microns because of the gas diffusion through the material. Also, the pressurized-cell type of detectors only recorded the first penetration in each detector.

To overcome these factors, the capacitor-type penetration detector was proposed in 1957. The operation of the capacitor detector, unlike that of the pressurized-cell detector, depends on phenomena created during the impact and penetration of the meteoroids. Since meteoroid impacts could not be simulated in the laboratory, a recoverable flight experiment offered the best means of establishing the exact operation of the detector. Two factors led to the conclusion that this flight experiment could be a short-duration (several minutes) probe-type experiment. First, the capacitor detector could be used to record penetrations in very thin materials. Second, the then best available estimates of the meteoroid-penetration rates to expect in such thin materials indicated that hundreds of penetrations would be experienced in several minutes. The Whipple 1956 flux-mass estimate (ref. 3) was used in designing the experiment. This estimate is shown in figure 1. The penetration calculations were made with the penetration equation derived by Kinard and Collins in reference 4. Specifically, penetration measurements were to be made in 6.5, 20, and 45 microns of the plastic film. The area of the experiment was planned to be 20 square meters and the exposure in space was estimated to be 300 seconds. Approximately 1500 penetrations were expected to be recorded during

the experimental flight. By recovering the detectors after the flight, some of the meteoroid penetrations could be located possibly with meteoroid material still embedded in the crater; thus chemical and spectral analysis of the material would be possible.

An inflatable paraglider was chosen as the spacecraft because it could be folded into a small volume for launch, it could inflate and create a large surface area for exposing the penetration detectors, and it offered a means of recovering the detectors. Since such paragliders were being considered also as a means of recovering other objects, such as launch-vehicle stages from space, the tracking of the glider during the reentry was expected to provide valuable performance data.

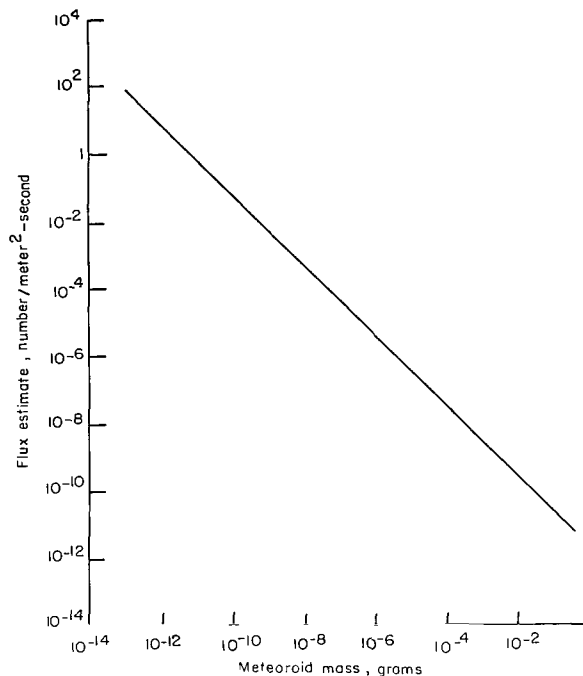


Figure 1.- Estimate of meteoroid flux (ref. 3).

CAPACITOR PENETRATION DETECTOR

General Description

The capacitor-type meteoroid penetration detector is essentially one or more charged thin-film capacitors. When a high-energy particle penetrates the dielectric of the capacitors, a significant amount of material is vaporized and possibly ionized in the area of the penetration. As a result, the penetrated capacitor is momentarily shorted and partially discharged. The current flow resulting from this discharge can then be monitored to indicate the penetration events. The ionization dissipates in less than a microsecond, allows the capacitor to recharge, and thus enables the detector to sense repeatedly the micrometeoroid penetrations. The specific detector used in this experiment consisted of multiple capacitors of aluminized poly(ethylene terephthalate) (PET) dielectric laminated together as shown in figure 2. Three layers of 6.5-micron

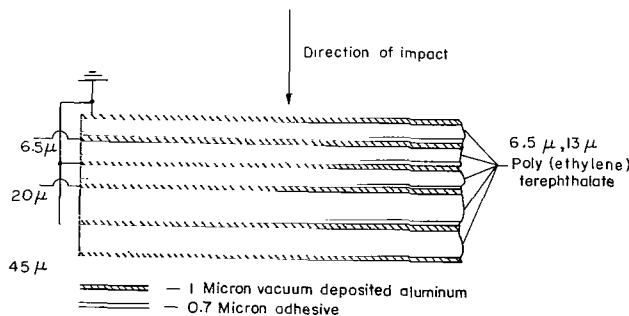
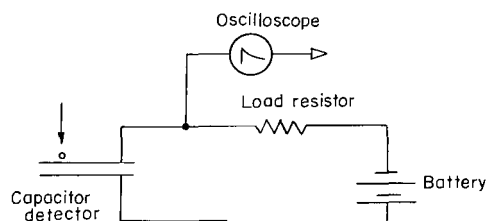
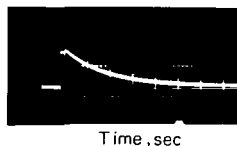


Figure 2.- Cross section of multilayer capacitor-type detector.

aluminized PET and two layers of 13-micron aluminized PET were laminated together with approximately 0.7 micron of adhesive. The second, fourth, and sixth aluminized surfaces were biased (with a 30-volt dc potential); thus, micrometeoroid penetrations could be detected at depths of 6.5 microns, 20 microns, and 45 microns. The other aluminized surfaces were grounded to prevent capacitance coupling of signals from penetrated capacitors to unpenetrated capacitors. Since the aluminized surfaces and the adhesive made up only a small part of the total detector thickness, the flux measurements are considered to be only in the respective various thicknesses of PET and not in a composite of PET, aluminum, and adhesive.



(a) Circuit diagram.



(b) Sample oscilloscope trace of capacitor discharge.

Figure 3.- Typical capacitor-detector circuit.

The circuit used to monitor the capacitor discharges consisted of a 30-volt dc battery source which charged the capacitor through a 50-kilohm resistance as shown in figure 3(a). The capacitor-charging current was monitored by measuring the voltage drop across the 50-kilohm resistor with an oscilloscope (see fig. 3(b)). The resistance of the aluminized conductive surface was 2 ohms/meter or less and had little effect on the circuit performance.

Impact Test

Although micrometeoroid impacts cannot be fully simulated in the laboratory, laboratory tests were performed to identify the parameters affecting the sensor performance and to establish reasonable limits for the meteoroid-impact sensor performance. Impact tests on the multilayer capacitor

sensors were performed by using light-gas guns and conventional powder guns at the hypervelocity impact range at the Langley Research Center; a shaped-charge test facility at the Ballistic Research Laboratories (BRL); and the SSL Mark IV exploding-wire gun, a particle accelerator at North American Aviation, Inc. (NAA). The latter facility was not available until after the flight. Descriptions of these facilities are contained in references 5, 6, and 7, respectively. Table I lists the test conditions in the facilities.

The tests conducted at the hypervelocity impact range at the Langley Research Center involved the acceleration of projectiles many times the size of the meteoroids that were expected to penetrate the detectors in space, and the impacts of these projectiles resulted in holes having diameters that were several orders of magnitude larger than the detector thickness. Impacts through only the first and second capacitors had to be simulated by locally removing the back capacitor at the point of impact. In the tests

at the Langley Research Center, essentially all the impacts resulted in almost complete detector discharge. Both metallic and nonmetallic projectiles were used with similar results. These tests indicated that the impact velocities had to be above approximately 2 km/sec for the detector to function.

The shaped charges used in the detector test at the Ballistic Research Laboratories accelerated a cluster of iron fragments to velocities of about 6 km/sec. The fragment sizes varied from 1 to 500 microns and they were approximately cubic. The detector-penetration signals in these tests could not be identified with an individual particle but instead were the result of many particle penetrations. In each test the cluster of particles produced a near-complete discharge of the capacitor.

The studies which were conducted at North American Aviation, Inc., with the SSL Mark IV exploding-wire gun involved the acceleration of one or several 50- μ -diameter spheres to velocities as high as 15 km/sec. The SSL Mark IV was not utilized until after the flight test; however, tests were performed in this facility to aid in analyzing the flight data since this facility more nearly simulated the meteoroid impacts expected in space. The signals observed across the charging resistor when the detectors were penetrated by single, small projectiles varied from 5 to 70 mV; thus, when penetrations occurred nearer to the threshold, only a very small percent of the total capacitor charge is released. These tests also indicated that the amount of charge released may be influenced by the impact velocity. In general, more charge was released by penetrations of higher velocity particles than by penetrations of lower velocity particles. The impact tests performed in the exploding-wire gun also indicated that increasing the capacitor potentials is desirable. Reference 8 treats this observation in more detail.

In essentially all the tests performed, the detector discharge was observed to be temporary and the detectors did recharge and were capable of detecting additional penetrations. Additional data on tests performed on multilayer capacitor-type penetration detectors and on other capacitor-type penetration detectors are contained in reference 8.

Detector Construction

Capacitance-grade PET film was used as the detector dielectric. The capacitor plates were formed by vacuum deposition of aluminum. One side of each PET film was deposited with approximately 0.7 to 1.0 micron of aluminum, with the exception of one 13- μ -thick film that was aluminized on both surfaces as shown in figure 2. The aluminized PET films were laminated roll-to-roll into a continuous strip 0.3 meter wide. (See fig. 4.) The adhesive thickness was maintained at 0.7 micron or less by accurate control of adhesive concentration and the rate of application. The adhesive is basically a thermosetting polyester.

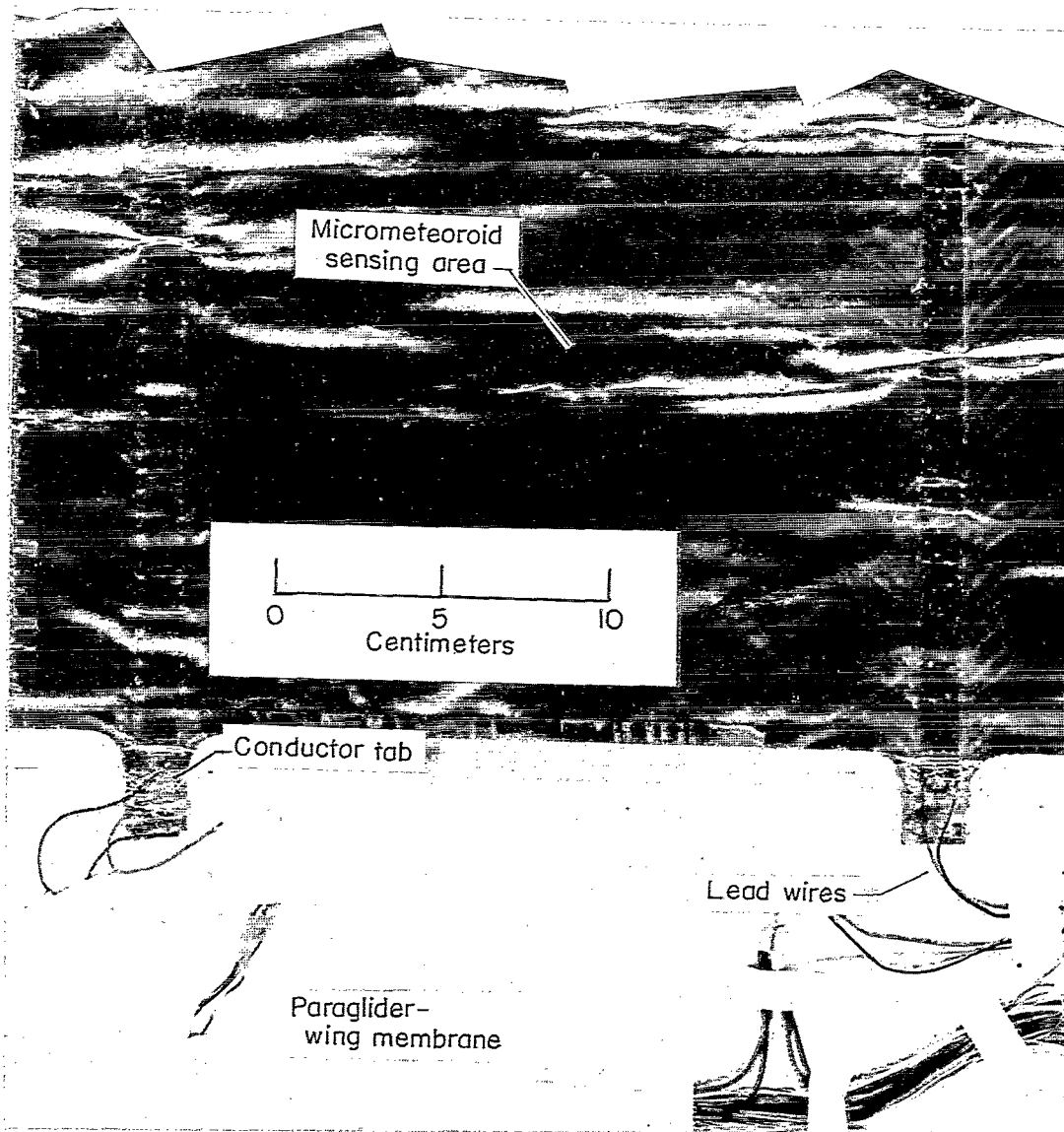


Figure 4.- Micrometeoroid detector and wiring layout. L-68-817

A narrow conductor strip of 12- μ -thick aluminum foil was introduced between each layer of aluminized PET so that it made electrical contact with the adjacent aluminum surface, and thus provided a means of connecting electrical leads to each aluminized surface. (See the schematic cross section in fig. 5.) The conductor strips were first perforated with a rotating wire brush to produce numerous surface burrs or protrusions much like that of a "carrot grater." In the lamination process these protrusions penetrated the adhesive layer used to bond the conductor strip and made a pressure contact with the aluminized surface. The contact resistance was found to be consistently less than 1 ohm. The lead wires were attached to the conductor strips by soldering with a standard 60/40 resin core solder. The use of silver-loaded epoxies and conductive cements to attach the electrical leads was tried, but the results were found to be unreliable.

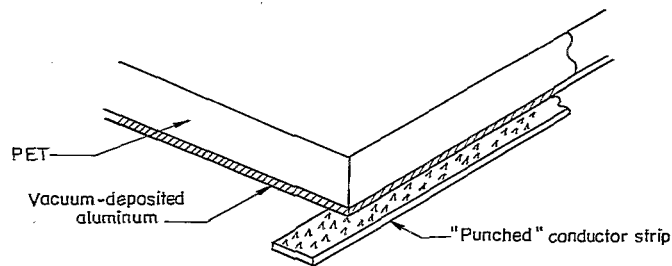
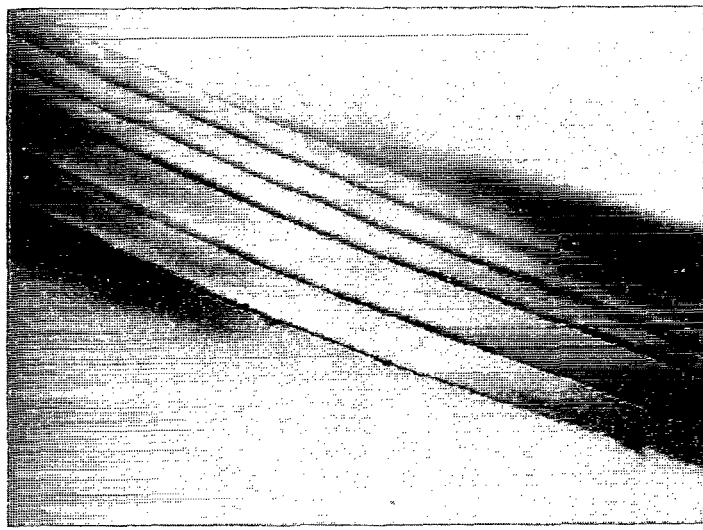


Figure 5.- Exploded schematic of detector material and conductor strip.

Quality control of the total detector thickness, the vacuum-deposited aluminum thickness, and the adhesive thickness was accomplished by microscopic visual examination of microtome sections of the laminated material. A microscope equipped with a micrometer eyepiece was used to make absolute measurements of the material thicknesses. A microphotograph of a typical microtome cross section is shown in figure 6. The conductor strips are not shown.



L-68-818
Figure 6.- Microphotograph of sensor cross section. X 570.

Detector Environmental Testing

The multilayer detectors as a component were subjected to severe tests to insure their ability to be folded for launch, to survive the launch loads, to be deployed, and to survive the space environment. The sensors were also qualified after being mounted on the spacecraft, as discussed in a later section.

The sensor-component test involved temperature cycling, vacuum, and flexing. During many of these tests, the sensors were biased and their electrical properties monitored. The physical conditions and the electrical properties of the detectors were checked after the completion of each of the tests to insure that no damage had occurred.

Sample detectors were subjected to temperatures ranging from approximately -180° C to 100° C. No defects that could affect the detector operation were noted. The flexibility tests, which were run to insure that the sensors could be folded and deployed, consisted of drawing a sample detector back and forth over a 3-millimeter-diameter rod while alternately immersing it in boiling water and liquid nitrogen. Again, no adverse effects were observed. Sample detectors were also subjected to several hours of thermal-vacuum (10^{-2} N/m²) tests without adverse effects.

SPACECRAFT

General Description

The spacecraft consisted of an inflatable paraglider, a 40-centimeter standard Aerobee extension section, and a standard Aerobee nose-cone section. The inflated paraglider and the extension section are shown in the photograph in figure 7. The paraglider provided a method for exposing the penetration detectors to the space environment and for recovering the detectors. Aerodynamic testing of the paraglider is treated in detail in reference 9. The 40-centimeter extension section housed the inflation system, an onboard camera, and a tracking beacon. The nose-cone section housed the electronic systems, the power system, the vehicle and spacecraft programmer, the telemetry system, and other components, as shown in figure 8.

The paraglider structure consisted of three inflatable tubes – a keel tube and two leading-edge tubes – each approximately 4.5 meters long. (See fig. 9.) The tube diameter at the apex section was 51 centimeters and tapered to approximately 20 centimeters at the trailing edge. A vertical tube 4 meters long and 40 centimeters in diameter connected the 40-centimeter extension section and the glider keel tube. This tube maintained the extension section and the attached nose cone in a fixed position relative to the wing. Four stainless-steel cables each 3 mm in diameter and wrapped with aluminumized glass fiber tape were strung between the paraglider wing-structure tube ends and the extension

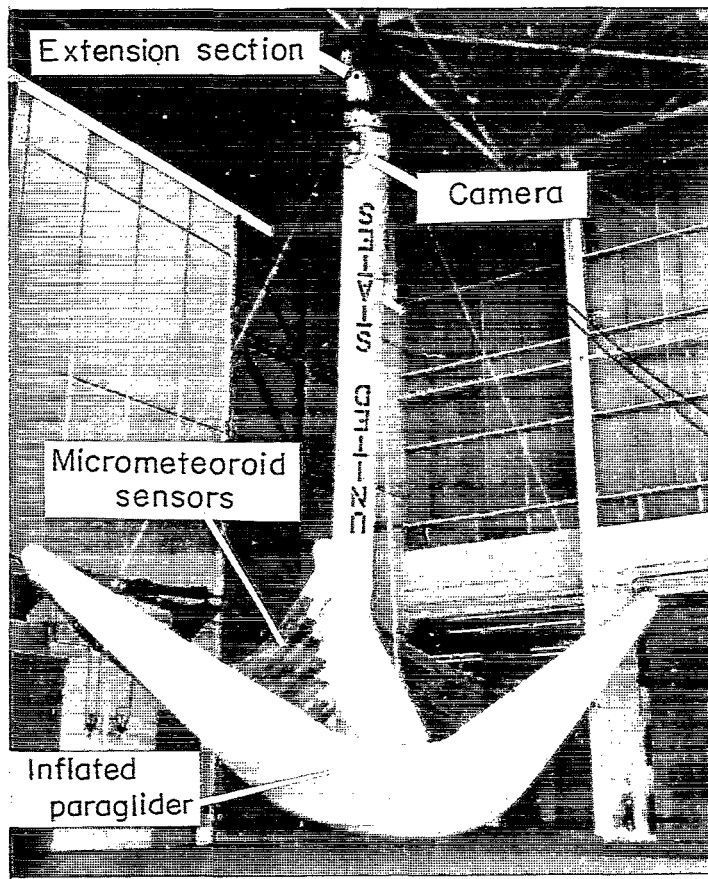


Figure 7.- Inflated paraglider.

L-68-819

section to act as load-carrying members during reentry. The wing membrane was attached to the wing keel and leading-edge tubes.

Paraglider Construction

The inflatable components of the paraglider were fabricated from a glass fiber cloth, which had been cleaned of the lubricant required in the weaving process and then impregnated, by using calendar rollers, with an uncured silicon elastomer. The glass fiber cloth provided the prime strength and the silicon elastomer provided a high-temperature gas barrier. Photographs of the basic fabric used in fabricating the inflatable components are shown in figure 10; the sections have been enlarged to show detail. This figure shows the outer layer of 285 g/m², 7 × 7 mesh (threads per cm) glass fiber cloth, the white silicon elastomer and the inner layer of a lighter weight 100 g/m², 16 × 8 mesh glass fiber cloth. Figure 11 shows the various paraglider components in an expanded-assembly drawing. Each component was fabricated by laying up the cloth on

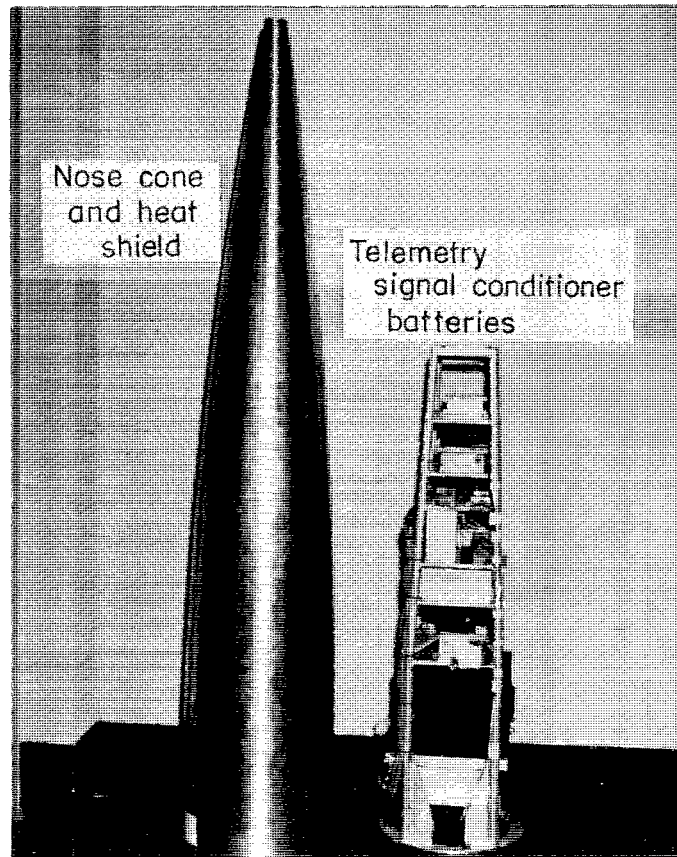


Figure 8.- Aerobee 150 nose cone and telemetry system. L-68-820

hard-core molds. Sheets of the same silicon elastomer used to impregnate the cloth were used as an adhesive.

A single layer of the basic fabric, as described and shown in figure 10, was used in the leading-edge booms, keel boom, and vertical tube. Along the leading edges a two-layer fabric construction was laid with a 125-micron elastomer adhesive. The apex section was fabricated in a similar fashion by using the two layers of elastomer fabric plus adhesive. The lap joint seams were taped by using the basic fabric and elastomer adhesive. The end caps of the leading-edge and keel booms were also constructed in a similar fashion by using a hemispherical hard-core mold. The forward end cap on the keel boom contained an aluminum attachment plate and air vent for attachment to the apex tube. The vertical support tube contained a similar plate for attachment to the keel tube. Both joints were then faired in with fabric as shown in figure 11.

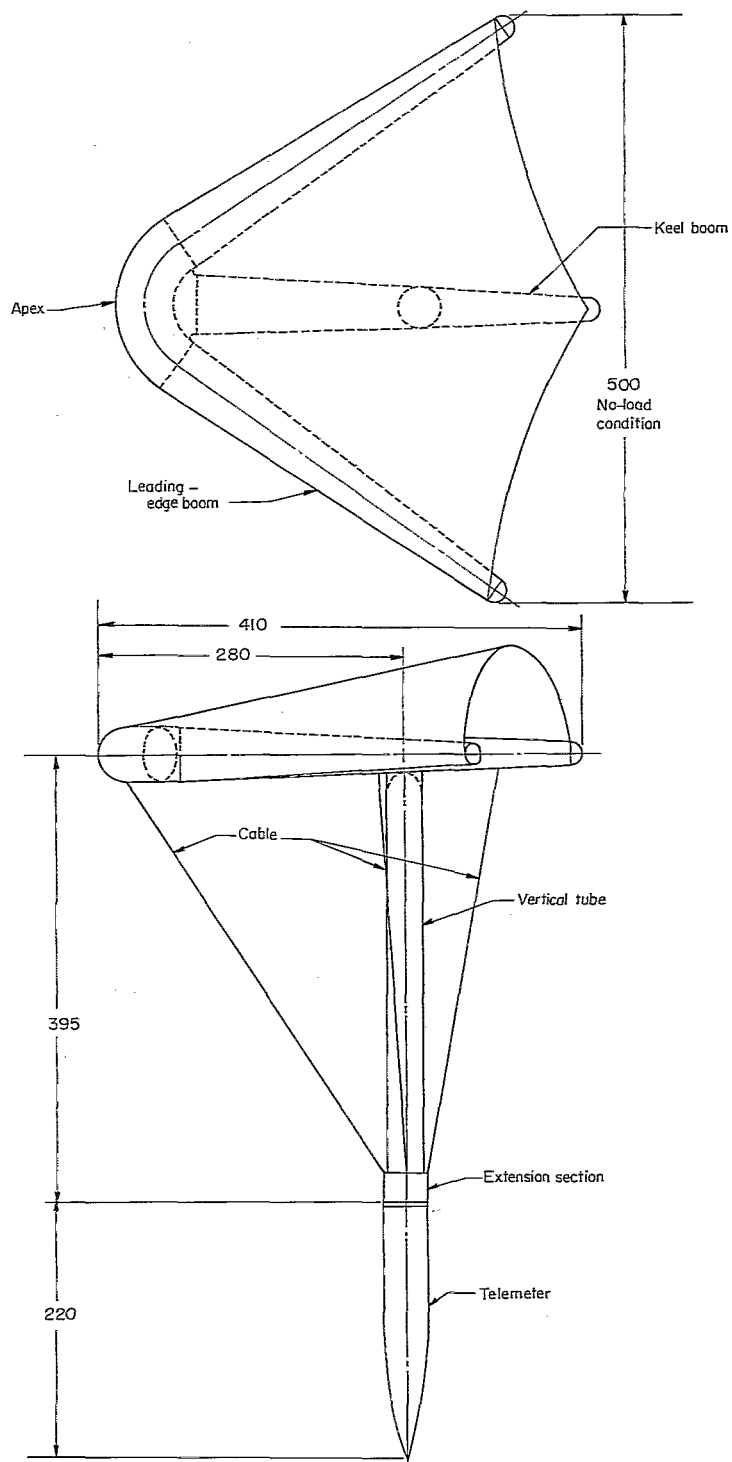
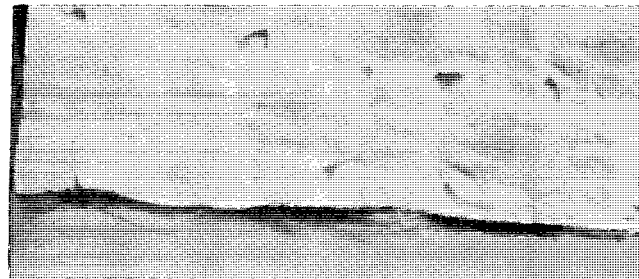
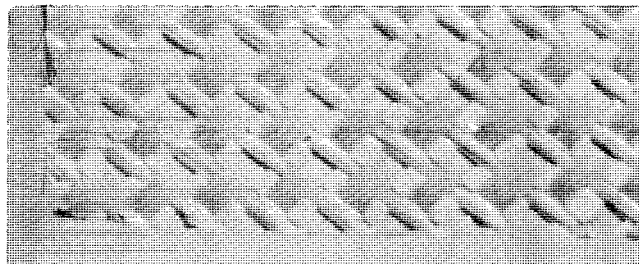


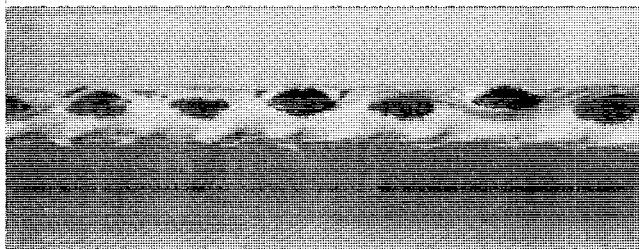
Figure 9.- Schematic of paraglider. All dimensions are in centimeters.



(a) Outer surface.



(b) Inner surface.



(c) Cross section.



Figure 10.- Enlarged sections of paraglider fabric.

L-68-821

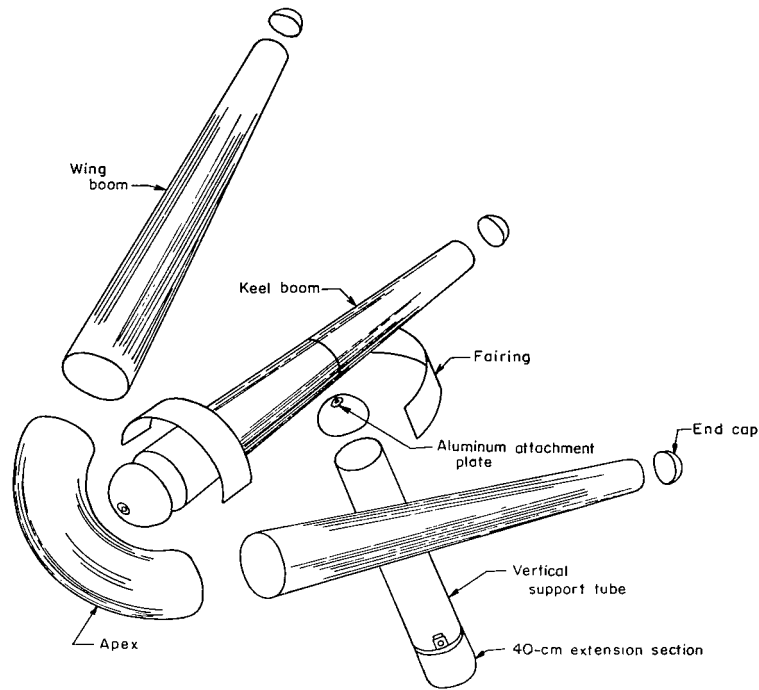


Figure 11.- Exploded view of paraglider inflatable tubing.

The wing membrane was made of glass fabric with a pressure-sensitive adhesive laminated to both the upper and lower surfaces. This pressure-sensitive adhesive was used to bond the meteoroid sensors to the membrane.

Four stainless-steel cables, each 3 millimeters in diameter and wrapped with aluminized glass fiber tape as a heat insulator, were strung as shown in figure 9. These cables acted as the principal load-carrying members between the wing and the 40-centimeter extension section during reentry and terminal flight.

Paraglider Testing

The paraglider materials, fabricated components, and fully assembled paraglider were tested to insure their ability to survive the flight environments.

Material tests.- The basic fabric was tested for tensile strength by using ASTM methods and a tensile strength tester. Sample joints and seams typical of those used in the paraglider were also tested in a similar manner. These tensile tests were performed both at room and at elevated temperatures. The high-temperature tests were conducted by enclosing the sample and the tensile-tester clamping jaws in an oven. Samples of the fabric were repeatedly folded and then tested to indicate the weakening effect of folding.

The basic fabric and elastomer were also subject to biaxial-loading tests at elevated temperatures by using the test facility shown in figure 12. The blower and air heaters shown provided 700° C air at a rate of 6400 cc/sec. The fabric sample was mounted by a clamping ring so that only the edges were supported. In each test the samples were pressurized to $13.8 \times 10^2 \text{ N/m}^2$. The test thermal cycles were as follows: a 60-second temperature rise to 620° C, a 20-second exposure at this temperature, and a 60-second cooldown. These temperatures and exposure times were representative of the calculated reentry-heating cycle. The cables were also tensile tested at elevated temperatures to insure their load-carrying capability.

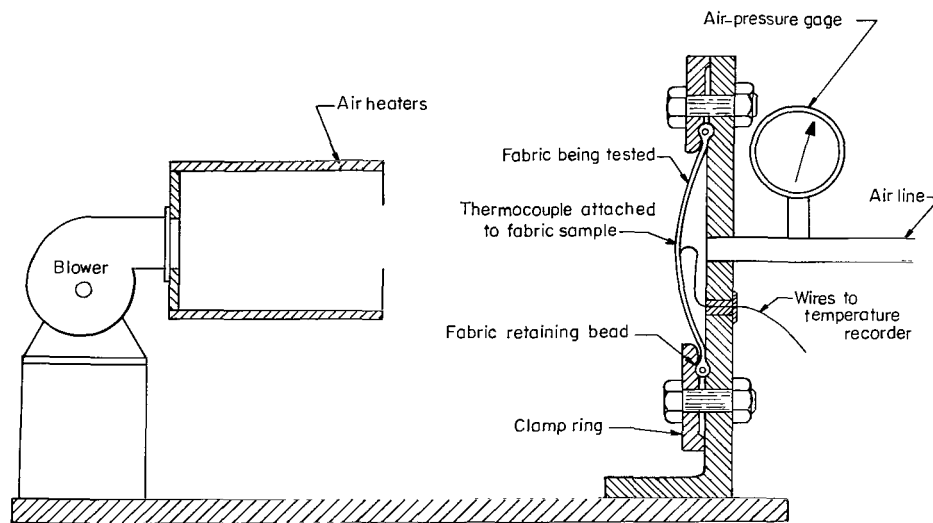


Figure 12.- Schematic of biaxial loading tester.

Component tests.- Tests on the two leading-edge booms and the single keel boom of the paraglider were conducted at both ambient and high-temperature conditions. A boom was tested as a cantilever by supporting it at the larger end and by applying a load perpendicular to the boom center line at the free end. Load-deflection determinations were made at 2.5 , 5.5 , and $9.0 \times 10^4 \text{ N/m}^2$ internal-tube pressures and at ambient and elevated temperatures up to 600° C. Quartz tube heaters were used to elevate the temperature. The vertical tube was tested in a similar fashion. The apex was tested by rigidly mounting the center-tube segment of the apex and by applying bending and rotational loads to the outer-tube segment. The apex was also tested at ambient temperature and at temperatures up to 600° C. Samples of each component part of the paraglider were tested under pressure to the bursting point. The bursting pressure was $9 \times 10^4 \text{ N/m}^2$; and resulted in a safety factor of approximately 1.5.

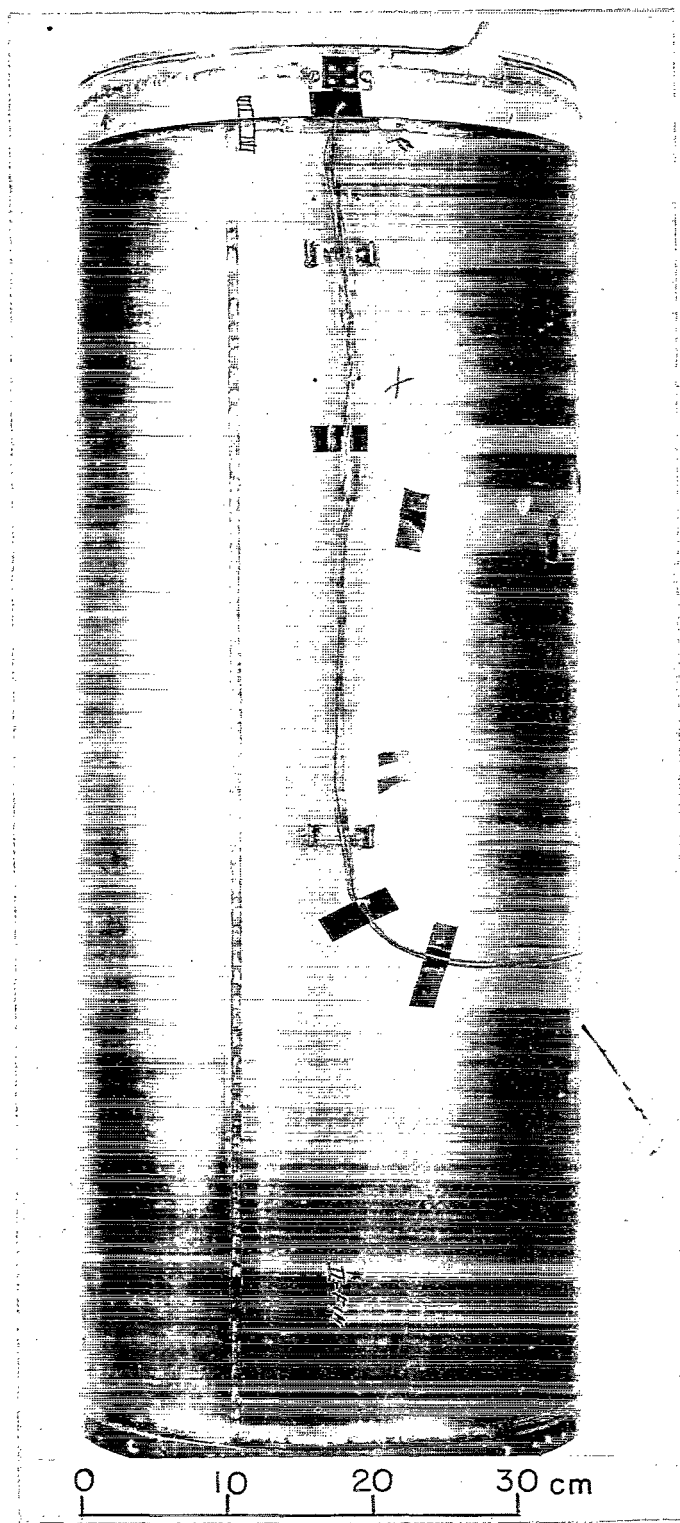


Figure 13.- Canister used in vacuum-tank test of paraglider. L-68-822

Paraglider test. - The assembled paraglider was tested to determine its structural characteristics when pressurized and its shaping modes when deployed from the packed condition. These tests were conducted at 10^{-2} N/m² in the 60-foot (18.2 m) vacuum sphere at the Langley Research Center. The paraglider was folded and packed in a canister (fig. 13) and then deployed in the vacuum sphere. High-speed motion-picture photography was used to record the shaping characteristics. These tests also indicated, as did the testing of the basic fabric, that folding and packing the paraglider weakens the fabric at the fold lines. As a result, the flight paraglider was packed a minimum number of times.

Packaged paragliders were vibration tested to determine the effects of the launch conditions. The structural and environmental tests run on the assembled spacecraft included biasing the sensors and monitoring for discharges and shorts that might be produced by the simulated launch and deployment tests. Considerable electrical noise was observed during these tests; however, the noise subsided after the launch and deployment tests of the spacecraft. Thus, a quieting of the sensor electronics would be expected after complete inflation of the spacecraft.

Spacecraft Packaging Separation and Deployment System

The series of photographs shown in figure 14 show the general sequence by which the inflatable part of the spacecraft was packed for the launch phase of the experiment. Initially, the paraglider was laid out (fig. 14(a)) and deflated to remove most of the residual air. Wooden "clothespin-type" clamps were used to hold the proper fold lines during deflation and folding. The wing surface and booms were folded accordion style from the apex to the vertical-tube intersection. The trailing edge was then folded to the vertical-tube intersection (figs. 14(b) and 14(c)). Finally, the wing booms, membrane, and the vertical tube were folded accordion style so that the final package (fig. 14(d)) was approximately 40 centimeters in diameter and less than 100 centimeters long. The folded paraglider was then wrapped with a protective aluminum shield the halves of which were held in place by removable pins. This assembly was then placed inside a standard 1-meter Aerobee extension section, the plastic guide rails on the aluminum shield being allowed to dovetail with matching guide rails in the extension section. Finally, the shield-retainer pins were removed.

A linear-shaped charge technique was used in deploying the paraglider after launch. The linear-shaped charge was wrapped around the circumference of the paraglider-extension section at the forward and aft ends of this section. Additional charges were placed longitudinally on the sides of the 1-meter section, 180° apart. The entire spacecraft, consisting of the telemeter nose section, the 40-centimeter inflation-system extension, and the paraglider 1-meter section, was then attached to the Aerobee 150 launch vehicle.

After launch and at the programmed altitude the charge was detonated, the entire spacecraft was separated from the launch vehicle, and the 1-meter paraglider extension section was separated into two halves as shown in figure 15. The halves of the aluminum protective shield that were dovetailed with the 1-meter extension section remained with this extension section, and thus, freed the paraglider to inflate. The retro rockets on the Aerobee 150, also shown in figure 15, were fired simultaneously with the charge to assist in separation of the spacecraft and the Aerobee 150 sustainer. This additional separation velocity reduced the possibility of contact between the burned out Aerobee sustainer and the inflating paraglider.

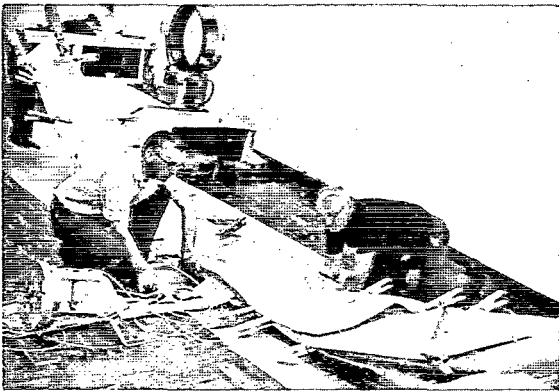
After the data period of the experiment was completed, a second linear-shaped charge was programmed to detonate and separate the telemeter nose section from the paraglider 40-centimeter extension section, and thus reduce the reentry loads. This charge failed to detonate.



(a) Initial layout and deflation.



(b) Primary folding.



(c) Intermediate folding.



(d) Final folded configuration in protective shield.

Figure 14.- Paraglider packing sequence.

L-68-823

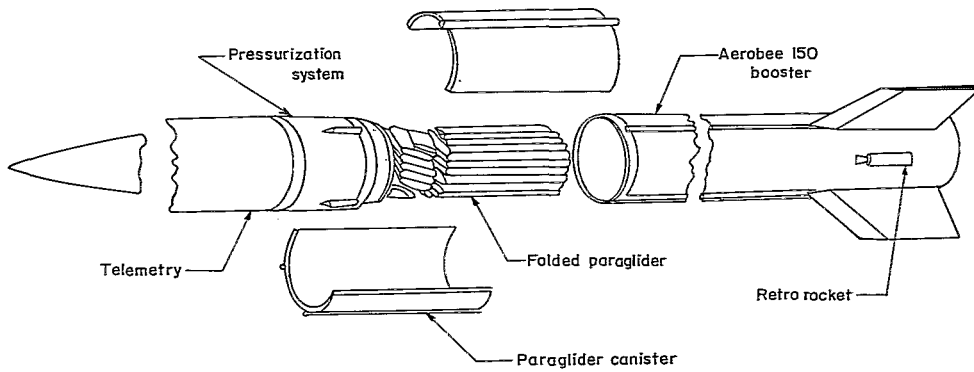


Figure 15.- Schematic of vehicle and payload.

Inflation System

A schematic of the paraglider inflation system is shown in figure 16. The inflation system was located in the 40-centimeter extension section between the paraglider-support tube and the nose section. A 0.017-cubic-meter tank pressurized with nitrogen to $4 \times 10^7 \text{ N/m}^2$ was used to supply the gas to pressurize the paraglider structural tubes. The pressurization cycle was initiated by opening the fill valve on command from the spacecraft programmer. The maximum flow rate through this fill valve was limited by the orifice shown upstream of the valve. During the first pressurization, however, the flow-control valve directed the gas flow through a second and smaller orifice which further limited the flow and prevented the paraglider from being shaped so rapidly that structural damage might result. The paraglider was first pressurized to $2 \times 10^4 \text{ N/m}^2$ and maintained at that pressure during the time the spacecraft was out of the atmosphere and gathering micrometeoroid data. The $2 \times 10^4 \text{ N/m}^2$ pressure-regulator switch controlled either the fill valve or the relief valve as needed to maintain this pressure.

For reentry $5.5 \times 10^4 \text{ N/m}^2$ internal pressure was required to prevent buckling of the structural tubes by the air loads on the wing. Consequently, just prior to reentry, the $5.5 \times 10^4 \text{ N/m}^2$ pressure switch was programmed to take control of the fill valve and the relief valve and to maintain the pressure at $5.5 \times 10^4 \text{ N/m}^2$. At the same time, the flow-control valve was programmed to bypass the small orifice because the already shaped paraglider pressure could be raised at a much faster rate than permitted by the small orifice and because the use of a slower rate would necessitate reducing the time allowed for gathering meteoroid data. A tube pressure of $5.5 \times 10^4 \text{ N/m}^2$ was neither required nor desired during the meteoroid-data-gathering portion of the flight, as it would have decreased the confidence of successfully completing the prime meteoroid experiment objective. Undetected damage to the glass fiber in the paraglider tubes might have resulted during the packing of the glider for launch; consequently, the lower pressure was used to increase the margin of safety for the tubes. The relief valve prevented the

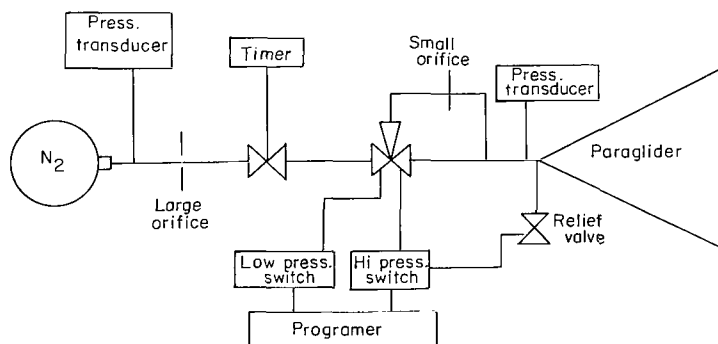


Figure 16.- Schematic of inflation and pressurization system.

overpressurization of the glider as the tubes and internal nitrogen were aerodynamically heated during the reentry.

Camera

A 16-mm sequence camera was also located in the 40-centimeter extension section and was used to photograph the separation, deployment, and reentry of the paraglider.

The camera was turned on at a speed of six frames per second after the payload separated from the booster. A 9-mm wide-angle lens and a mirror were used to obtain a large field of view. A photograph of this camera, lens, and mirror assembly is shown in figure 17. Figure 18 is a schematic of the camera location and the lens viewing angle. The front-surface mirror was placed in front of half of the camera lens at a 45° angle to the lens axis. The mirror extended from the lens axis to the outer edge of the field of view. One-half of the camera frame covered the reflected image in the mirror by having a look angle of approximately 90° to the paraglider-vertical-support tube. A series of photographs were taken by the camera and a discussion of these photographs is given in a later section.

Mounting and Wiring of Penetration Detectors

Nine strips of the multilayer-capacitor penetration detectors were bonded to the surface of each half of the wing membrane as shown in the schematic in figure 19. These strips are also shown in the photograph in figure 4. Thirty-six detector strips were thus

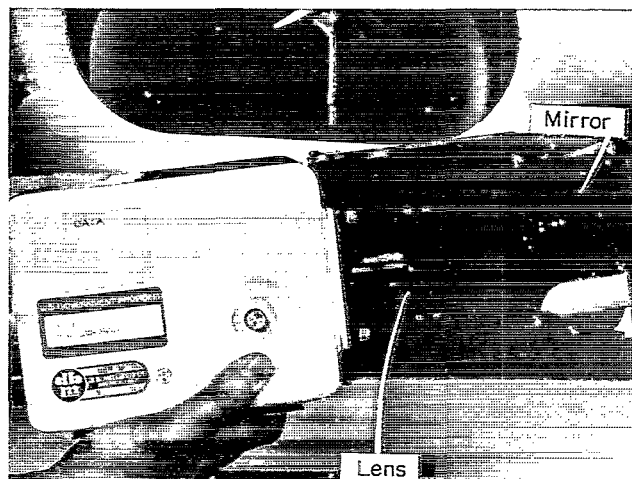


Figure 17.- Onboard 16-mm camera.

L-68-824

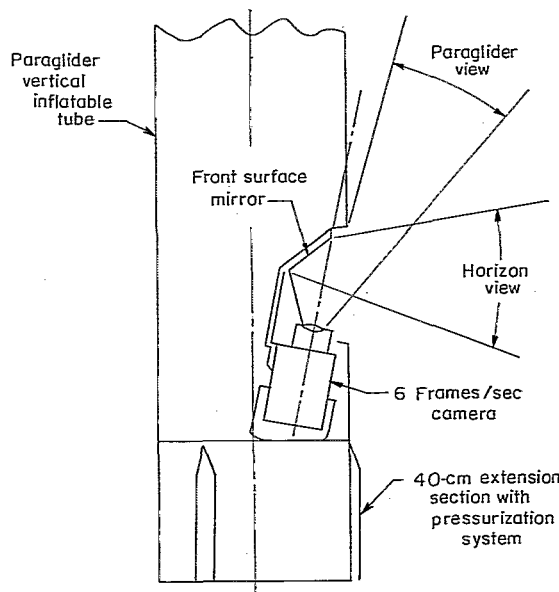


Figure 18.- Schematic of onboard camera.

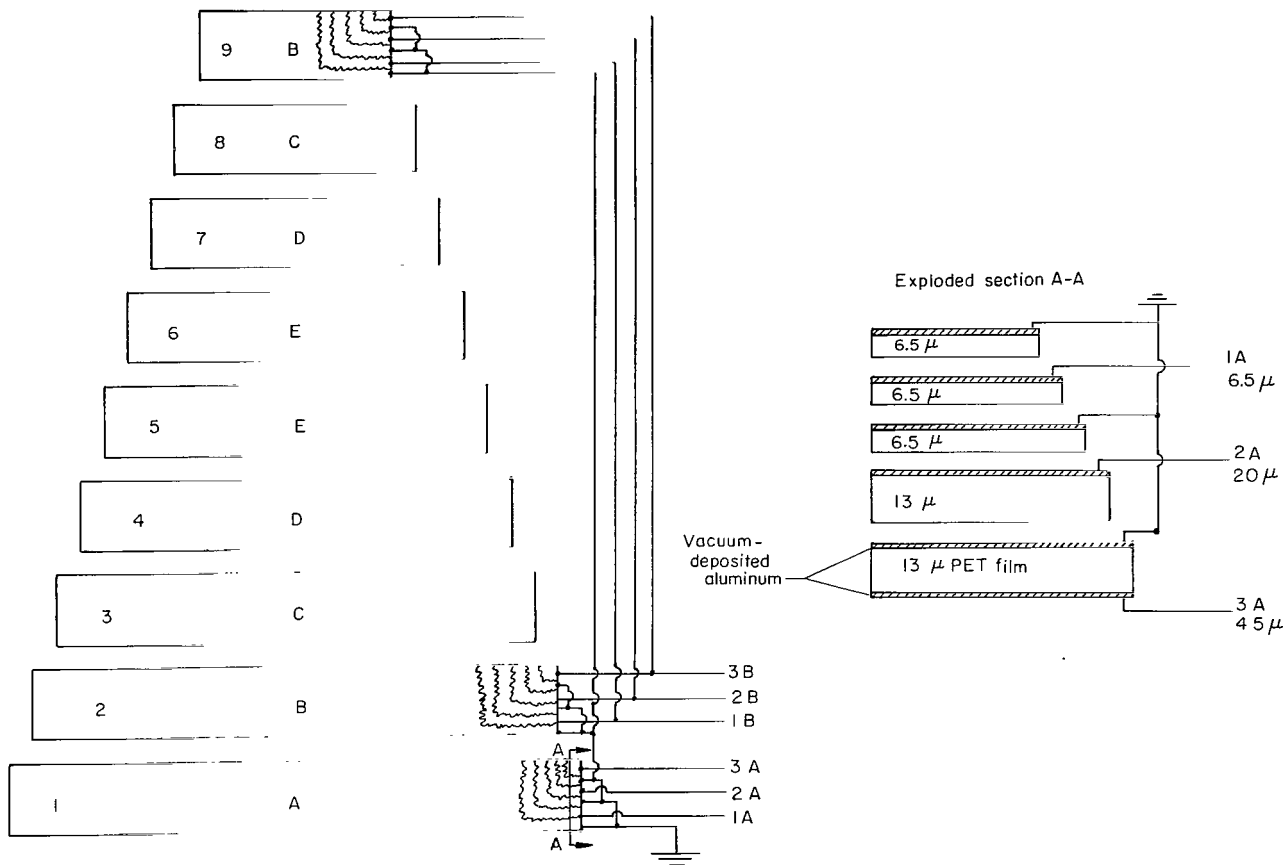


Figure 19.- Penetration-sensor wiring diagram.

mounted on the entire wing. The capacitors in these 36 strips were electrically connected to form 20 electrically separated detectors, 5 on each surface of each half of the wing. These five detectors, each having a surface area of approximately 1 square meter, are identified as A to E in figure 19. Strip no. 1 forms a single detector. Strips 2 and 9 have the capacitors at the respective depths wired in parallel, strips 3 and 8, 4 and 7, and 5 and 6 are connected in the same manner. All the ground plates of each detector were connected to a common ground lead. Each biased plate of each detector had a separate lead, which ran through the vertical tube to the signal-conditioning circuits in the nose-cone section. This wiring arrangement resulted in 60 biased leads and 1 common ground lead.

Penetration-Detector Signal Conditioning

The electronics for the penetration-detector signal condition were located in the Aerobee nose section as shown in figure 8. The leads from the biased plates at 6.5-, 20-, and 45-micron depths in each of 20 isolated detectors were connected to the plus terminal of separate batteries (fig. 20). The negative terminal of each battery was

connected through separate 50-kilohm resistors, labeled R_1 , to the spacecraft ground. A voltage drop across any one of the R_1 resistors, which would result from a meteoroid penetration, would be detected as a voltage drop across the R_2 resistor also shown in figure 20. Separate batteries, resistors, and other components were used to isolate each capacitor and prevent unpenetrated capacitors from rapidly recharging penetrated capacitors and thus attenuating the penetration-signal levels. By using three different preamplifiers and telemeter channels for each depth of penetration detected, penetration signals ranging from 0.002 volt to 30 volts could be resolved. This resolution, based on the detector laboratory-test data, appeared to cover any expected performance.

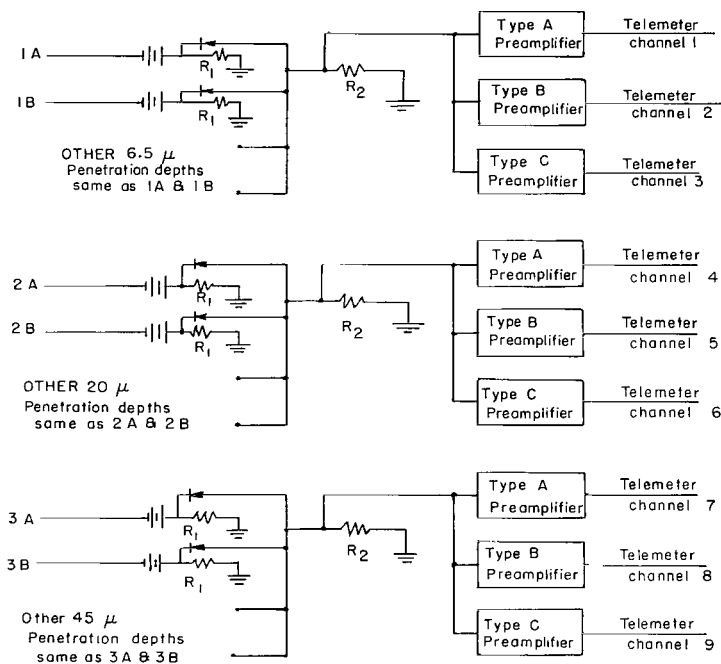


Figure 20.- Penetration-sensor circuit.

Telemetry Power and Sequencing Systems

A photograph of the telemetry system, power supply, and associated hardware is shown in figure 8. All the systems shown were housed in the 2.25-meter ogive nose. A pulse-position-modulator (PPM) telemetry system was used in this flight experiment to obtain all penetration data and systems performance. The Goddard Space Flight Center designed and supplied the telemetry system, detector biasing subsystem, and the spacecraft sequencing system, and managed the acquisition of all telemetered data during launch, flight, and reentry. The pulse-position-modulator system contained a

total of 16 channels for data acquisition. Table II lists all the telemetry channels and the respective data obtained from each. Channels 1 to 9 were used to obtain the meteoroid-penetration data. Channels 10 to 16 were used to acquire paraglider-inflation pressures and vehicle performance.

LAUNCH VEHICLE

The micrometeoroid paraglider spacecraft was launched from White Sands Missile Range by an Aerobee 150 rocket. This vehicle is a liquid-propellant single-stage rocket with a solid-propellant booster rocket, which provides an initial acceleration to a velocity of approximately 60 m/sec. The thrust characteristics, specific impulse, and general payload capabilities of the Aerobee 150 are given in reference 10. Figure 15 shows the general launch-vehicle configuration, the only modification to the standard Aerobee 150 vehicle consisting of a retrorocket system to assist in payload separation. The Aerobee 150 is spin-stabilized by canted sustainer-stage fins. A standard despin system is provided to despin the vehicle after burnout of the sustainer. The despin system consists of two cold-gas jets mounted near the thrust face of the sustainer. The residual gas used to pressurize the Aerobee liquid engine fuel is used as fuel in the despin system. The despin jets are controlled by a roll-rate gyroscope.

RESULTS AND DISCUSSION

Spacecraft Trajectory

The objective of the program was to obtain micrometeoroid-penetration data in PET above the earth's sensible atmosphere. Thus, the maximum obtainable altitude and as long an exposure time as possible at altitudes above 120 km were desired. The 120-km altitude is not exact but an approximate altitude above which the low-mass particles should not have been slowed or destroyed by entry into the earth's atmosphere. Originally, an exposure time of about 300 seconds was planned; however, an increase in the payload final weight reduced the maximum attainable altitude and the exposure time.

The Aerobee 150 rocket (designated 4.67 NP) was launched from site L-21 at the White Sands Missile Range on June 10, 1964, at 05 hours, 44 minutes, 59 seconds MST. The vehicle was launched 2° off the vertical, due north. The ideal 0° vertical launch was prohibited by range safety. A plot of the altitude-range trajectory is shown in figure 21, and a plot of the velocity and altitude against time is shown in figure 22. The flight-trajectory data were obtained by a tracking radar. Burnout of the single-stage Aerobee occurred at 52.5 seconds after launch at an altitude of 36.5 km and at a velocity of 1.49 km/sec. The launch vehicle and spacecraft coasted to an altitude of 93 km at $T + 96.5$ seconds. The despin of the vehicle occurred during the coast period.

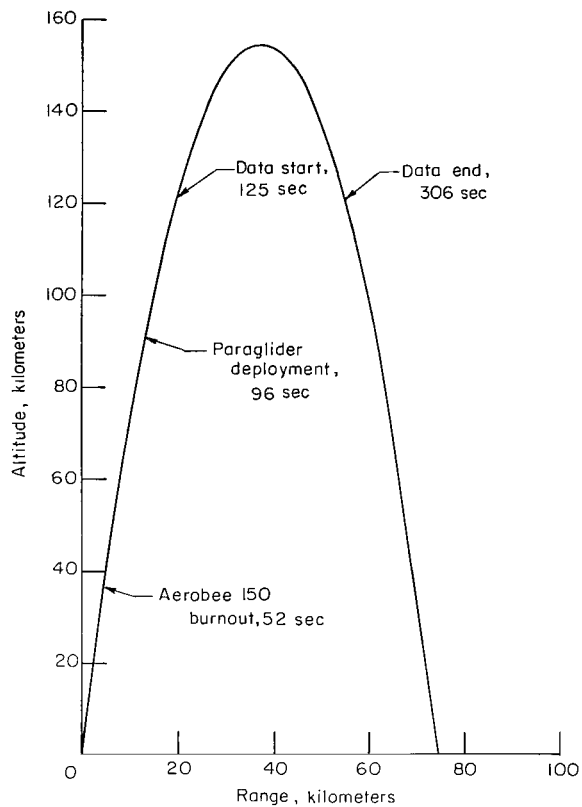


Figure 21.- Altitude-range trajectory.

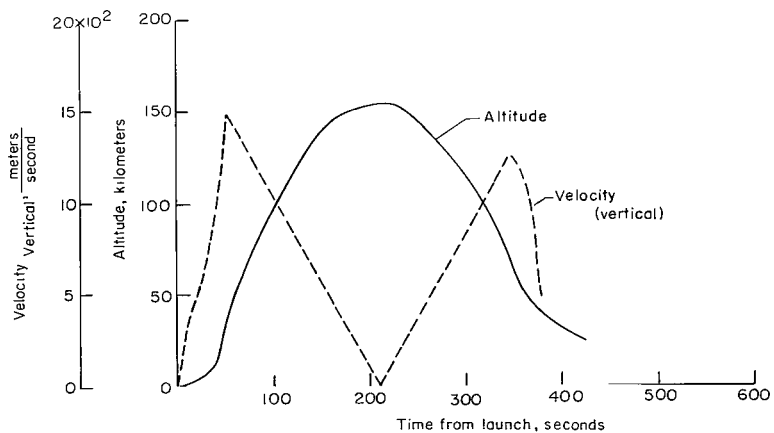
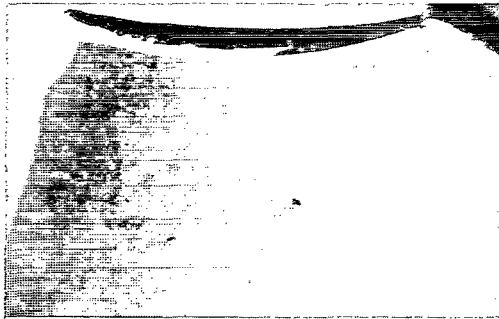
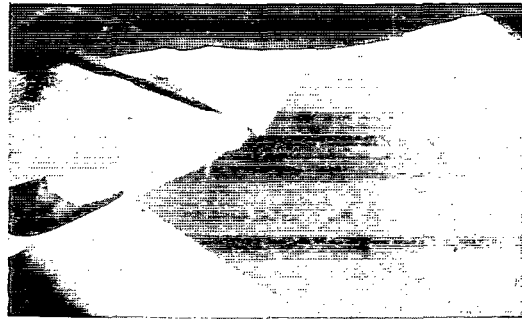


Figure 22.- Trajectory for velocity and altitude plotted against time.

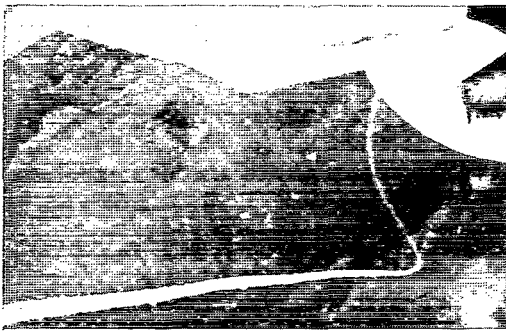
Separation and deployment occurred at $T + 96.5$ seconds as programmed. The 16-mm camera, as discussed earlier, was used to photograph both the inflation of the paraglider and the horizon. A series of these photographs are shown in figures 23 and 24. Only



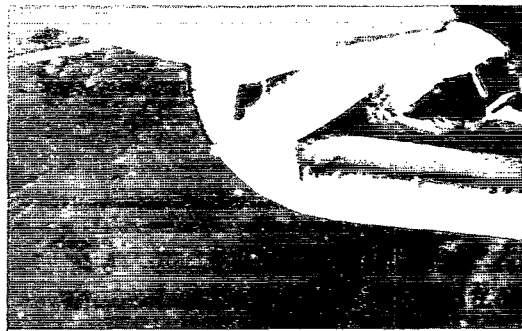
(a) $T + 97$ seconds.



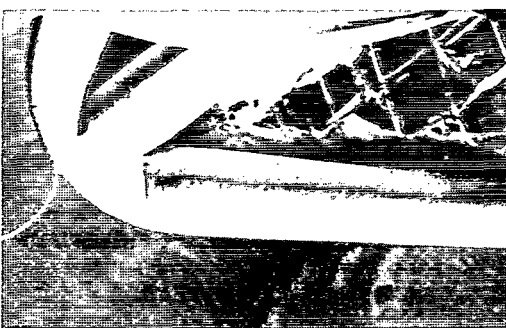
(b) $T + 99$ seconds.



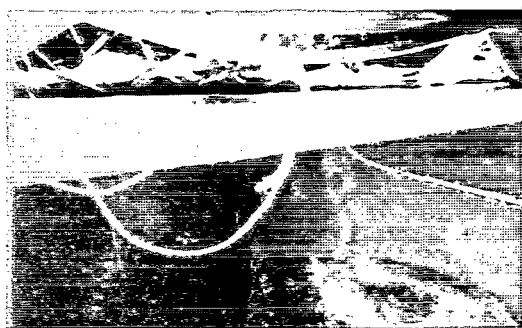
(c) $T + 101$ seconds.



(d) $T + 103$ seconds.



(e) $T + 105$ seconds.



(f) $T + 107$ seconds.

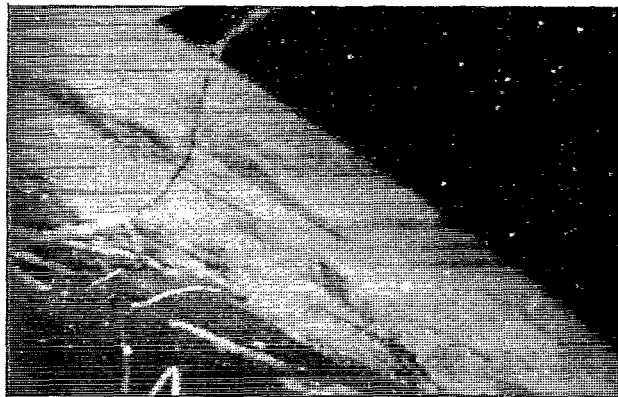
Figure 23.- Onboard-camera photographs of inflatable-micrometeoroid-paraglider deployment.

L-68-825

the half of the frame viewing the paraglider is shown in the photographs in figure 23. The photograph in figure 23(a) was exposed just prior to inflation. The remaining photographs (figs. 23(b) to 23(f)) show the inflation process. The maximum altitude attained by the spacecraft was 154.7 km and occurred at 211 seconds after launch. The telemetry nose section was programmed to release at $T + 306$ seconds at approximately 115 km and thus resulted in a total exposure time of 191 seconds. As discussed earlier, the nose-cone-severance system failed to operate. Spacecraft impact occurred 74.5 km down-range at 831 seconds after launch.

Spacecraft Orientation

To expose equal areas of the detectors in all directions the paraglider should attain a random motion. The approximate sensor orientation with respect to the earth achieved by the spacecraft was determined from both onboard-camera photographs of the earth's horizon and the shadows on the spacecraft, and photographs of the spacecraft taken with a ground-based telescope camera. A sequence of earth-horizon photographs taken with the onboard camera is shown in figure 24. A series of photographs taken with the radar-controlled telescope camera (fig. 25) shows several events throughout the flight. The spin rate was determined from the movement of the vertical tube's shadow across the wing in the onboard-camera film. This rate was measured at two points during the data period and was found to be approximately 0.04 revolution per second. The paraglider was deployed in an inverted position with the nose cone up and the wing down. This attitude was confirmed by the positions of the paraglider in figures 25(b) and 25(c), which were taken 7 seconds and 18 seconds, respectively, after deployment. The angle between the plane of the sensors and the earth surface is approximately 10° to 20° . This angle is approximated by measuring the position of the paraglider on the telescope-camera film and by observing the relative position of the horizon on the onboard-camera film. This angle increases to approximately 70° to 80° , 144 seconds after launch or about halfway between start of data and apogee. After this point the camera resolution is not sufficient to resolve the shape of the paraglider. Figure 25(d) shows the paraglider at apogee. For the entire data period, the wing-oriented photographs from the onboard camera show a portion of the earth's surface or horizon; thus, the paraglider remained in an inverted position relative to the earth. This condition indicated that the angle between the wing plane and the earth did not exceed 90° . From the changing position of the earth's horizon in the onboard-camera photographs, the paraglider appeared to have had a large cone angle about the center of gravity and vertical-support-tube axis. The shape of the paraglider could again be resolved at about 270 seconds after launch or about halfway between maximum altitude and the end of the data period. At this time the wing plane angle with the earth was nearly 45° and still inverted.



(a) T + 196 seconds.

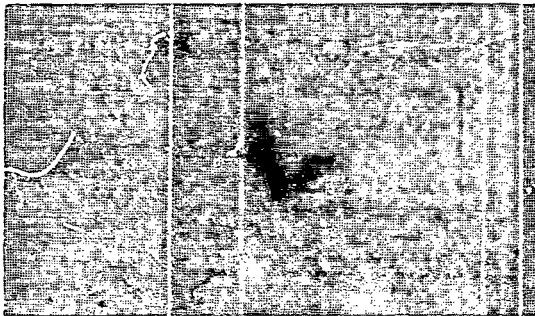


(b) T + 143 seconds.

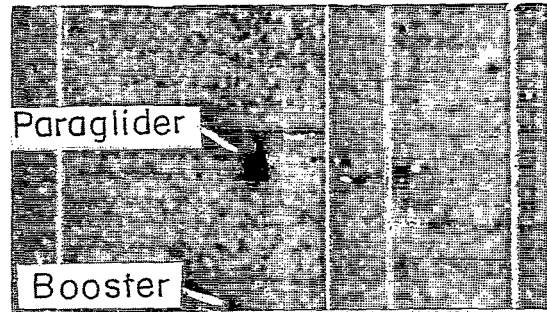


(c) T + 104 seconds.

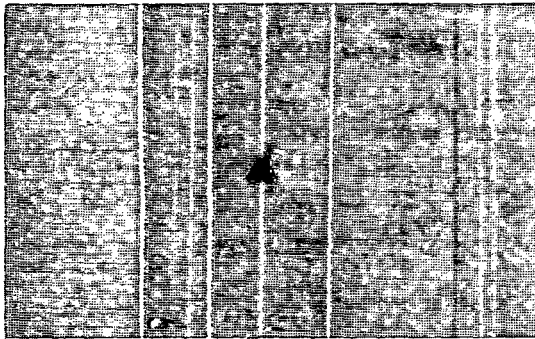
Figure 24.- Earth-horizon photographs. L-68-826



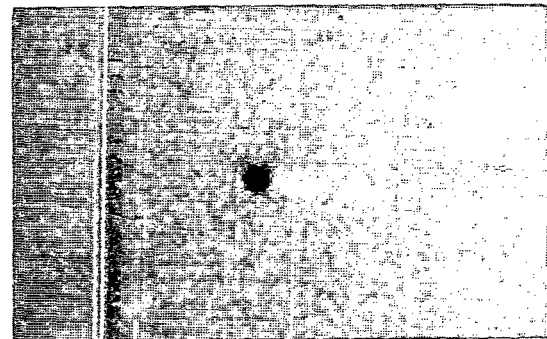
(a) Retro, 97 seconds.



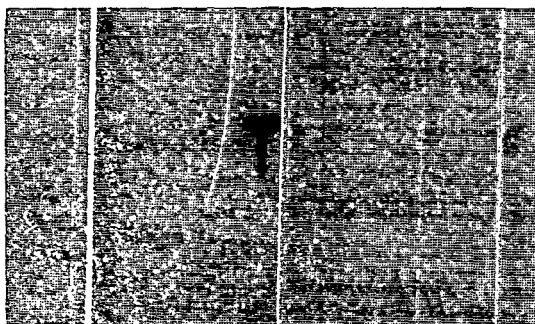
(b) 104 seconds.



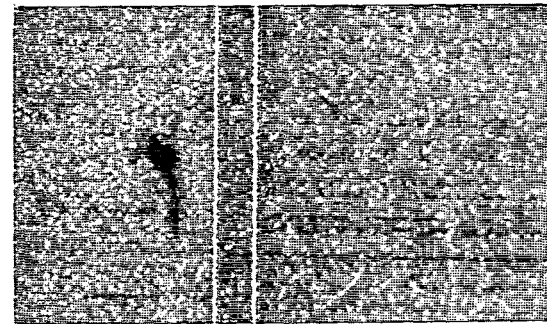
(c) Data start, 115 seconds.



(d) Apogee, 211 seconds.



(e) 351 seconds.



(f) 461 seconds.

Figure 25.- Sequence of photographs taken with radar-controlled telescope camera.

L-68-827

Penetration Data

No indications of penetrations in the 20- or 45-micron capacitor detectors were found; however, indications in the 6.5-micron detectors were noted. Thus, no particles of sufficient energy to penetrate 20 or 45 microns of PET film were encountered. The analysis of the data for the 6.5-micron detector was difficult and uncertain for two reasons. Considerable discharging of the capacitor developed during launch and deployment, and no well-defined separation could be made between the discharges resulting from deployment and those resulting from micrometeoroid impacts. This discharging of the capacitor during launch and deployment was also observed in the ground tests of simulated deployment, and, consequently, was expected during the actual flight. Such deployment discharges are thought to be caused by the motion of the paraglider wings and the flexing of the detectors during inflation.

The ground tests also indicated that the capacitors would become electrically quiet (except for possible micrometeoroid impacts) and the launch and deployment noise would end before $T + 115$ seconds or approximately 20 seconds after deployment. The onboard camera indicated that the paraglider was fully deployed and the wings stable at $T + 115$ seconds; however, the detectors remained noisy with no well-defined quieting period after deployment. The discharging of the capacitor after deployment was approximately two orders of magnitude greater than that expected from the meteoroid flux. At approximately $T + 125$ seconds, some of the discharging characteristics that were present during launch and deployment were no longer observed; thus, penetration data are read from this time on.

The penetration indications in the 6.5-micron detectors fall into several levels of activity. (See tables III and IV.) The indications tabulated are only those with signal levels exceeding the maximum telemeter background noise of about 5 mV, and, therefore, range from 8 to 300 mV. None of the discharges of the sensors appeared to exceed 1 volt. Recent ground test data seem to indicate that capacitor-type sensors should have voltage potentials of 80 to 100 volts to produce well-defined penetration discharges when impacted by particles of low mass. From 131 seconds to 267 seconds after launch (with the exception of approximately a 15-second period starting at about $T + 150$ seconds) 21 penetrations through the 6.5-micron detectors were observed. These indications (table III) occurred on the average of one about every 7 seconds. A typical portion of the telemeter record for this period is shown in figure 26(a). For the 15-second period starting at 150 seconds after launch, penetration indications were observed at the extremely high rate of 10 to 20 per second. (See table IV.) Part of the telemeter record showing this high rate of discharge is given in figure 26(b). No penetration indications were observed from 267 seconds after launch until the end of the experiment. Figure 27 illustrates the levels of penetration activity as a function of spacecraft position along the trajectory.

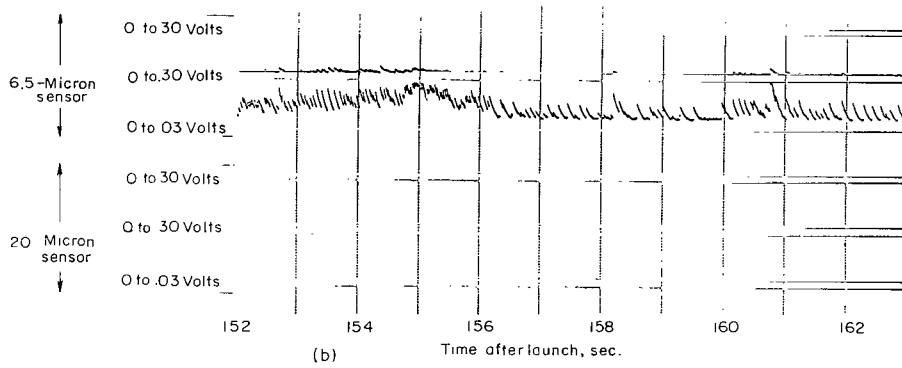
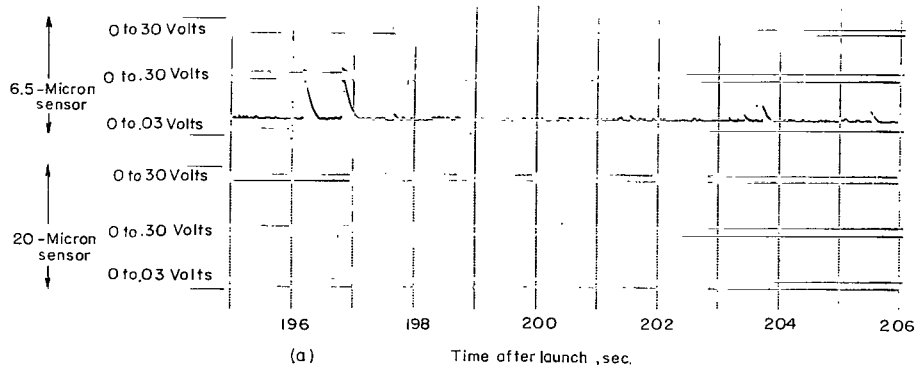


Figure 26.- Telemeter printout of micrometeoroid sensor.

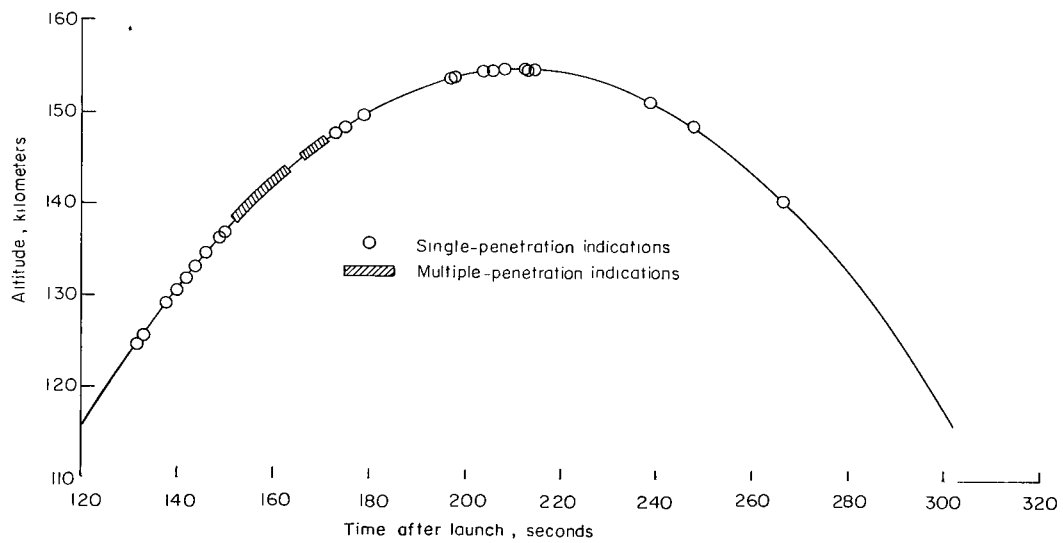


Figure 27.- 6.5 μ detector-penetration indications.

Analysis of the described data indicated three possibilities of micrometeoroid activity but, unfortunately, the data from this experiment alone cannot identify the true situation. First, all the penetration indications observed possibly resulted from valid meteoroid penetrations. Several factors could explain the peculiar distribution of events. Most of the penetrations were observed during the ascent portion of the trajectory. This fact could result from what is believed to be an unlikely situation; namely, that the particles have low velocities and, thus, the spacecraft-velocity reaction during ascent was required for penetration of the thinnest detectors. The very rapid penetration rate observed for the brief period after $T + 150$ seconds of flight time could have resulted from a cluster of fragments striking the spacecraft. A single meteor breaking up could have produced a spray of small particles. A second possibility is that this rapid sequence of penetration indications from $T + 150$ to $T + 165$ seconds resulted from an electrical breakdown and arcing in one capacitor, and that only those penetration indications contained in table III are valid. The third possibility is that all the penetration indications resulted from electrical breakdown and arcing in the 6.5-micron capacitors, and at approximately $T + 267$ seconds the electrical faults in the capacitors burned out, the capacitors cleared, and only then did they become stable with no meteoroid penetrations being detected.

In examining meteoroid data obtained from other experiments, conflicting evidence can be found to indicate that both meteoroid penetration should have been observed (refs. 11 and 12) and that meteoroid penetrations should not have been observed (refs. 2 and 13). Figure 28 compares the data obtained by the micrometeoroid paraglider experiment with data obtained by other experiments. Two penetration rates have been calculated from the data of this experiment and they are shown in figure 28. The highest rate was calculated by assuming that all the penetration indications are valid meteoroid penetrations. The lower rate was calculated by assuming that only those penetration indications shown in table III are valid. An upper limit for the penetration rate was calculated by assuming that the detectors only became operable after $T + 267$ seconds and that no meteoroid penetrations were detected. The equation (from refs. 14 and 15)

$$P = e^{-\psi At} \quad (1)$$

where

P probability of no penetrations

ψ meteoroid flux, $\frac{\text{Number of penetrations}}{\text{m}^2\text{-sec}}$

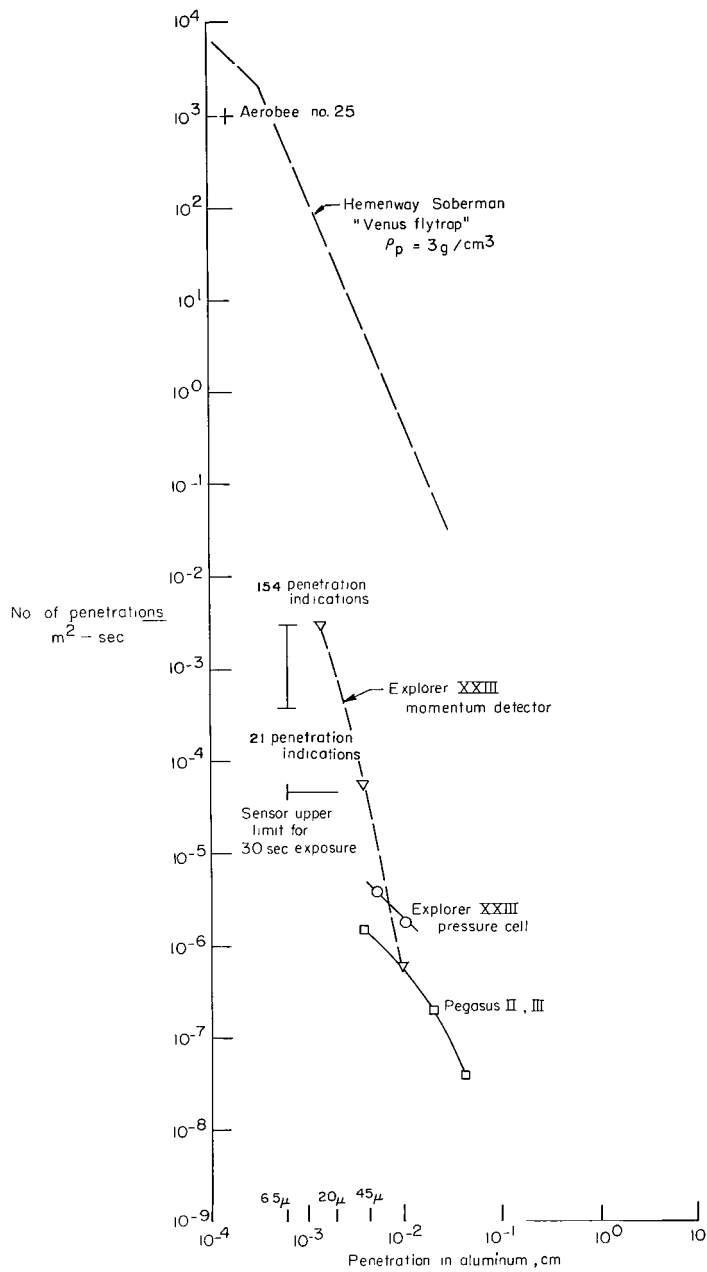


Figure 28.- Penetration-flux estimates in aluminum when shielded by the earth from one-half of meteoroid flux.

A area, m²

t time, sec

was used to determine the upper limit for an area of 18 m², and an effective exposure time of 30 seconds. The upper limit shown in figure 28 was calculated for an arbitrary P of 1 percent.

The data obtained from an earlier experiment (ref. 11) using an Aerobee high-altitude sounding rocket, specifically Aerobee 25, are shown in figure 28. Aerobee 25 used a photo-tube light cell to detect impact light flashes. These data indicate that a large number of penetrations should have been detected in the paraglider capacitor sensor. The momentum detectors flown on the Explorer XXIII spacecraft (ref. 2) also indicate the possibility that some hit indications should have been observed on the 6.5-micron sensor, whereas the pressure cells indicated that it should not. However, recent tests on the high-sensitivity microphone indicated some erroneous counting resulting from temperature changes, thus, an exact correlation is questionable. It should be kept in mind that these experiments were looking at different environments since the Aerokees are high-altitude sounding rockets and the Explorer XXIII was a long-duration orbiting spacecraft with a higher effective altitude. A flux measured by the Hemenway-Soberman "Venus flytrap" (ref. 12) is also shown in figure 28. This flux model also predicts that the sensors on the paraglider experiment should have detected thousands of penetrations.

On the other hand, an extrapolation of the data from the Explorer XXIII pressure-cell penetration detectors and the Pegasus capacitor-type penetration detectors indicates that no hit indications should have been observed on the paraglider experiment detectors. Here again, the Explorer and Pegasus are not measuring the same environment and the large number of hit indications observed could be representative of the low-altitude environment.

Less than 1 percent of the detector area was recovered and only a small part of that recovered was undamaged by the reentry heating. An examination of the undamaged recovered detector with a $\times 40$ stereo microscope did not disclose any penetrations or crater damage. No crater damage was expected from these observations, because the area recovered was located along the inner edges of the boom and apex and would have been shielded from most of the meteoroids.

Paraglider

The flight test on the paraglider demonstrated that a paraglider such as that described herein could be packed in a container with a diameter of 40 cm and a length of

100 cm and successfully deployed in the space environment. Complete inflation of the paraglider was accomplished in less than 20 seconds. As mentioned earlier, the inflation was recorded by the onboard camera and is shown in figure 23. At 306 seconds after launch, prior to reentry, a linear-shaped charge was programmed to sever the nose cone and telemetry package from the paraglider to reduce reentry loads and to allow a proper trim of the glider for reentry and terminal flight. The severance system failed to operate properly; however, as the aerodynamic loads increased, the paraglider did attain a proper flight attitude as determined by the photographs from the tracking telescope camera. The maximum aerodynamic pressure was calculated to occur at $T + 374$ seconds. The film from the onboard 16-mm camera indicated loss of wing membrane and also buckling of the wing boom at approximately $T + 375$ seconds. Wing-boom buckling would indicate excessive loads or loss of pressure or both. The paraglider failed at or near the time of predicted maximum aerodynamic heating and pressure. The recovered parts of the spacecraft are shown in figure 29.



Figure 29.- Micrometeoroid-paraglider payload after impact.

L-68-828



CONCLUSIONS

The excess noise on the sensor-telemeter channels prior to and after deployment, without a well-defined quiet period, makes the analysis of the micrometeoroid-penetration data difficult and uncertain. Other data obtained in this report have led to the following conclusions:

1. None of the discharges of the sensor appeared to exceed 1 volt. This fact would support much of the recent ground test data which indicate that capacitor-type sensors should have voltage potentials of 80 to 100 volts to produce well-defined penetration discharges when impacted by particles of low mass.

2. The capacitor-discharge rates were not uniform but rather erratic. These results are not consistent with recent satellite measurements but may be indicative of the low-mass particles in a localized near-earth environment.

3. A number of discharges were observed in the 6.5-micron sensor during the 169-second data period. During the same period of time, no simultaneous discharges occurred in the 20- and 45-micron capacitors of the multilayer detector. Thus, it is assumed that no particles of sufficient energy to penetrate 20 or 45 microns of plastic film were encountered.

4. Failure of the nose-cone-severance system to function properly caused the ultimate failure of the paraglider wing membranes and booms.

Langley Research Center,
National Aeronautics and Space Administration,
Langley Station, Hampton, Va., November 27, 1967,
124-09-14-02-23.

REFERENCES

1. Hastings, Earl C., Jr., compiler: The Explorer XVI Micrometeoroid Satellite – Supplement III, Preliminary Results for the Period May 27, 1963, Through July 22, 1963. NASA TM X-949, 1964.
2. O'Neal, Robert L., compiler: The Explorer XXIII Micrometeoroid Satellite. Description and Preliminary Results for the Period November 6, 1964, Through February 15, 1965. NASA TM X-1123, 1965.
3. Whipple, Fred L.: The Meteoritic Risk to Space Vehicles. Vol. I of Vistas in Astronautics, Morton Alperin and Marvin Stern, eds., Pergamon Press (New York), c.1958, pp. 115-124.
4. Kinard, William H.; and Collins, Rufus D., Jr.: An Investigation of High-Velocity Impact Cratering Into Nonmetallic Targets and Correlation of Penetration Data for Metallic and Nonmetallic Targets. NASA TN D-726, 1961.
5. Collins, Rufus D., Jr.; and Kinard, William H.: The Dependency of Penetration on the Momentum Per Unit Area of the Impacting Projectile and the Resistance of Materials to Penetration. NASA TN D-238, 1960.
6. Gehring, J. William, Jr.; and Richards, L. G.: Further Studies of Micro-Particle Cratering in a Variety of Target Materials. Hypervelocity Impact – Fourth Symposium, APGC-TR-60-39 (III), U.S. Air Force, Sept. 1960.
7. Scully, C. N.; Escallier, E. A.; Rosen, F. D.; and O'Keefe, J. D.: Electrothermal Gun for Hypervelocity Ballistics Research. Rept. SID-64-1156, North Am. Aviation, Inc., Nov. 17, 1964.
8. Broderick, John J.: Capacitor-Type Meteoroid-Penetration Sensors – Description and Test Results. NASA TN D-4524, 1968.
9. Croom, Delwin R.; and Fournier, Paul G.: Low-Subsonic Wind-Tunnel and Free-Flight Drop-Test Investigation of a Paraglider Configuration Having Large Tapered Leading Edges and Keel. NASA TN D-3442, 1966.
10. Anon.: Aeropees-Astropees, Sounding Rockets. Aerojet-Gen. Corp.
11. Berg, Otto E.; and Meredith, L. H.: Meteorite Impacts to Altitude of 103 Kilometers. J. Geophys. Res. (Letters to ed.), vol. 61, no. 4, Dec. 1956, pp. 751-754.
12. Hemenway, C. L.; and Soberman, R. K.: Studies of Micrometeorites Obtained from a Recoverable Sounding Rocket. Astron. J., vol. 67, no. 5, June 1962, pp. 256-266.


- 
13. Dozier, James B.: Meteoroid Data Recorded on Pegasus Flights. The Meteoroid Satellite Project Pegasus First Summary Report. NASA TN D-3505, 1966, pp. 65-76.
 14. Feller, William: An Introduction to Probability Theory and Its Applications. Vol. II. John Wiley & Sons, Inc., c.1966.
 15. Cramér, Harold: The Elements of Probability Theory. John Wiley & Sons, Inc., c.1955.

TABLE I.- IMPACT FACILITIES

Facility	Projectiles	Projectile velocity	Environment
Light-gas gun	1.5 mm aluminum, steel, glass spheres	4 to 5 km/sec	Vacuum, 10^{-1} N/m ²
Powder gun	1.5 mm to 6.0 mm aluminum, steel spheres	2 km/sec	Air and vacuum, 10^{-1} N/m ²
Shaped charge*	Up to 500 microns iron fragments	Up to 6 km/sec	Air and vacuum, 10^{-1} N/m ²
Electro-thermal gun	35 to 45 micron borosilicate spheres	10 to 16 km/sec	Vacuum, 10^{-2} N/m ²

*Particle sizes resulting from the detonation of a shaped charge with an iron core vary widely from extremely small to approximately 500 microns. Particles in the 50- to 100-micron range have velocities up to 6 km/sec, whereas the larger particles have lower velocities.

TABLE II.- TELEMETER CHANNELS

Channel	Function
1	Low-sensitivity 6.5-micron penetration sensor
2	Medium-sensitivity 6.5-micron penetration sensor
3	High-sensitivity 6.5-micron penetration sensor
4	Low-sensitivity 20-micron penetration sensor
5	Medium-sensitivity 20-micron penetration sensor
6	High-sensitivity 20-micron penetration sensor
7	Low-sensitivity 45-micron penetration sensor
8	Medium-sensitivity 45-micron penetration sensor
9	High-sensitivity 45-micron penetration sensor
10	Nitrogen inflation sphere pressure
11	Aerobee rocket-chamber pressure/paraglider tube pressure
12	Spin-rate gyro
13	Longitudinal accelerometer
14	Aerobee-rocket helium pressure
15	Despin event
16	Sustainer-separation event

TABLE III. - CUMULATIVE HIT INDICATIONS

Cumulative hits on 6.5-micron detector	Time after launch, sec	Discharge amplitude, volts
1	131.6	0.030
2	132.9	.010
3	137.3	.070
4	139.6	.010
5	141.4	*.300
6	143.2	.030
7	145.9	.020
8	148.5	.023
9	149.4	.008
10	178.6	.008
11	196.2	.025
12	196.8	.034
13	203.7	.011
14	205.5	.010
15	208.0	.008
16	212.3	.008
17	212.6	.017
18	214.6	.010
19	238.2	.020
20	247.4	.014
21	266.4	.028

*Discharge amplitude exceeded the 0- to 0.30-volt channel full-scale deflection but was not measurable on this channel.

TABLE IV.- MULTIPLE CUMULATIVE HIT INDICATIONS

Cumulative hits	Time after launch, sec	Discharge amplitude, volts	Cumulative hits	Time after launch, sec	Discharge amplitude, volts
1	151.7	0.013	41	154.3	0.017
2	151.8	.012	42	154.4	.057
3	151.9	.012	43	154.4	.028
4	152.0	.010	44	154.5	.025
5	152.1	.176	45	154.5	.008
6	152.1	.023	46	154.6	.028
7	152.2	.015	47	154.6	.014
8	152.2	.016	48	154.7	.011
9	152.2	.017	49	154.7	.008
10	152.3	.017	50	154.7	.025
11	152.3	.016	51	154.8	.025
12	152.4	.017	52	154.8	.023
13	152.5	.019	53	154.8	.017
14	152.6	.018	54	154.9	.040
15	152.7	.031	55	154.9	.034
16	152.8	.016	56	154.9	.042
17	152.9	.018	57	154.9	.034
18	152.9	.016	58	154.9	.031
19	153.0	.022	59	155.0	.034
20	153.0	.070	60	155.1	.034
21	153.0	.022	61	155.1	.025
22	153.1	.011	62	155.2	.020
23	153.1	.008	63	155.2	.020
24	153.2	.011	64	155.2	.017
25	153.2	.011	65	155.3	.017
26	153.3	.028	66	155.3	.023
27	153.4	.031	67	155.3	.017
28	153.5	.040	68	155.4	.014
29	153.6	.040	69	155.4	.014
30	153.7	.025	70	155.4	.018
31	153.7	.025	71	155.4	.020
32	153.8	.020	72	155.5	.017
33	153.8	.008	73	155.5	.011
34	153.9	.011	74	155.6	.011
35	153.9	.008	75	155.7	.011
36	154.0	.014	76	155.8	.014
37	154.0	.034	77	155.8	.011
38	154.1	.017	78	155.8	.011
39	154.1	.028	79	155.9	.008
40	154.2	.023	80	155.9	.017

TABLE IV.- MULTIPLE CUMULATIVE HIT INDICATIONS - Concluded

Cumulative hits	Time after launch, sec	Discharge amplitude, volts	Cumulative hits	Time after launch, sec	Discharge amplitude, volts
81	155.9	0.011	108	160.8	0.057
82	156.0	.014	109	161.0	.028
83	156.1	.020	110	161.1	.013
84	156.1	.011	111	161.2	.014
85	156.2	.014	112	161.8	.014
86	156.4	.017	113	161.9	.023
87	156.6	.011	114	162.1	.011
88	156.9	.012	115	162.3	.011
89	157.1	.008	116	162.4	.011
90	157.3	.011	117	162.6	.008
91	157.5	.011	118	162.8	.011
92	157.7	.011	119	166.1	.014
93	157.8	.012	120	166.2	.014
94	158.2	.025	121	166.4	.008
95	158.3	.011	122	166.5	.012
96	158.6	.008	123	167.5	*.300
97	158.8	.008	124	168.7	.011
98	158.9	.010	125	168.8	.008
99	159.5	.008	126	169.2	.008
100	160.0	.011	127	169.4	.013
101	160.1	.020	128	169.5	.028
102	160.2	.020	129	169.6	.200
103	160.3	.014	130	169.8	.008
104	160.4	.011	131	170.6	.011
105	160.5	.008	132	172.5	.014
106	160.5	.008	133	174.6	.008
107	160.7	.008			

*Discharge amplitude exceeded the 0- to 0.30-volt channel full-scale deflection but was not measurable on this channel.

FIRST CLASS MAIL

12U 001 39 01 3DS 68106 00903
AERONAUTICAL ENGINEERING LABORATORY/AFWL/
Kirtland Air Force Base, NEW MEXICO 87117

ATTN: MISS MADEIRA F. CANEVA, CHIEF TECHNICAL
LIBRARY /W1117

POSTMASTER: If Undeliverable (Section 158
Postal Manual) Do Not Return

"The aeronautical and space activities of the United States shall be conducted so as to contribute . . . to the expansion of human knowledge of phenomena in the atmosphere and space. The Administration shall provide for the widest practicable and appropriate dissemination of information concerning its activities and the results thereof."

— NATIONAL AERONAUTICS AND SPACE ACT OF 1958

NASA SCIENTIFIC AND TECHNICAL PUBLICATIONS

TECHNICAL REPORTS: Scientific and technical information considered important, complete, and a lasting contribution to existing knowledge.

TECHNICAL NOTES: Information less broad in scope but nevertheless of importance as a contribution to existing knowledge.

TECHNICAL MEMORANDUMS: Information receiving limited distribution because of preliminary data, security classification, or other reasons.

CONTRACTOR REPORTS: Scientific and technical information generated under a NASA contract or grant and considered an important contribution to existing knowledge.

TECHNICAL TRANSLATIONS: Information published in a foreign language considered to merit NASA distribution in English.

SPECIAL PUBLICATIONS: Information derived from or of value to NASA activities. Publications include conference proceedings, monographs, data compilations, handbooks, sourcebooks, and special bibliographies.

TECHNOLOGY UTILIZATION PUBLICATIONS: Information on technology used by NASA that may be of particular interest in commercial and other non-aerospace applications. Publications include Tech Briefs, Technology Utilization Reports and Notes, and Technology Surveys.

Details on the availability of these publications may be obtained from:

SCIENTIFIC AND TECHNICAL INFORMATION DIVISION
NATIONAL AERONAUTICS AND SPACE ADMINISTRATION
Washington, D.C. 20546